ACS APPLIED ENERGY MATERIALS
Cite This: ACS Appl. Energy Mater. XXXX, XXX, XXX−XXX
Article
www.acsaem.org

ZIF 67 Based Highly Active Electrocatalysts as Oxygen Electrodes in Water Electrolyzer

Shraboni Ghoshal,[†] Sarah Zaccarine,[‡] Grace C. Anderson,[†] Madison B. Martinez,[†] Katherine E. Hurst,[†] Svitlana Pylypenko,[‡] Bryan S. Pivovar,[†] and Shaun M. Alia*[,†]

[†]Chemistry and Nanoscience Center, National Renewable Energy Laboratory, 15013 Denver West Parkway, Golden, Colorado 80401, United States

[‡]Department of Chemistry, Colorado School of Mines, 164 Coolbaugh Hall, Golden, Colorado 80401, United States

Supporting Information

ABSTRACT: Mitigating high overpotential losses originating from the sluggish oxygen evolution reaction (OER) during water electrolysis is key to establishing a sustainable hydrogen generation technique. Herein we report a Co-imidazolate framework (ZIF 67) as an OER catalyst that exhibits high activity in both a three electrode cell and an electrolyzer. Additionally, Fe, Ni, and Zn have been incorporated into ZIF 67 to evaluate their effects on the OER activity of ZIF 67. Due to the high charge conductivity of ZIF 67, none of the reported catalyst was carbonized at high temperature, a process that is generally accompanied by significant mass loss. Hence, in addition to being highly active, these catalysts are scalable which makes them promising candidates for application in commercial power markets.

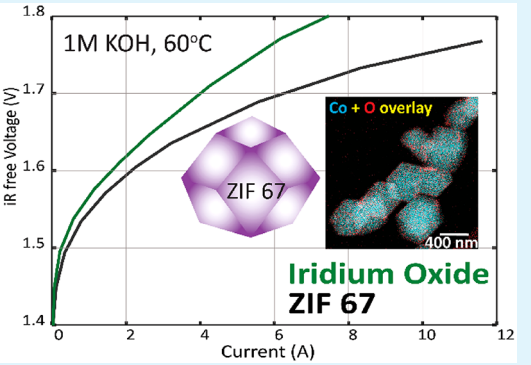

KEYWORDS: *oxygen evolution reaction, metal organic framework, ZIF 67, AEM electrolysis, non-precious-metal catalyst*

1. INTRODUCTION

Advantages such as high energy density, efficient energy storage, interconversion between chemical and electrical energy, and ease of handling make hydrogen a valuable commodity.[1] Additionally, hydrogen offers great flexibility in terms of generation (fossil fuels, solar, thermal, wind, etc.), scale (watts to gigawatts), and end use (electric grid, industry, transportation).[2] Electrochemical splitting of water is a promising route for hydrogen production due to facile hydrogen evolution reaction (HER) kinetics, the ability to operate the electrolyzer unit at low temperatures, tolerance to frequent startups and shut downs, and minimal water requirements (due to high energy density of H−H bond).[3] Compared to proton exchange membrane (PEM) based electrolyzers, anion exchange membrane (AEM) electrolyzers offer several advantages, including the ability to use non-platinum group metals and improved durability of catalysts and other system components (transport layers, flow fields, bipolar plates). Sluggish oxygen evolution kinetics at the anode, however, is a major source of loss in electrolysis.[4,5] Finding efficient catalysts is therefore critical to address the cost targets associated with hydrogen production and achieve desirable durability at low loadings. Non-precious-metal based catalysts have been developed as anodes in AEM electrolyzers, but finding highly efficient, scalable, durable, and cost-effective catalyst materials still remains a challenge.[6−8]

Among conventional anode catalysts like mixed metal oxides,[9−11] spinels,[12−16] and perovskites,[4,17,18] metal organic framework (MOF) based catalysts offer several advantages such as high surface area, controllable shape and size, and a porous network that aids in efficient inflow and outflow of electrolyte, reactants, and products.[19−22] Zeolitic imidazolate frameworks (ZIFs) are a subclass of MOFs and are considered to be excellent precursors for obtaining N-enriched high surface area carbon based catalytic materials with high activity and ability to resist poisoning and corrosion.[23] To achieve these traits, the ZIF based catalysts are heat treated at high temperatures of ca. 1000 °C.[24] The prevalent ZIF based catalyst synthesis strategy includes incorporating active metals such as Fe, Ni, and Co into the framework with subsequent pyrolysis at high temperature to obtain homogeneous distribution of active metals over a conductive carbon matrix.[25,26] While numerous highly active catalysts have been reported, such a synthesis strategy has a major drawback since a critical amount of mass loss is encountered during pyrolysis at a high temperature, challenging the scalability of the catalyst materials.[27] Additionally, significant loss in surface area is observed as a result of particle sintering.[28] These factors put a restriction on the scalability of catalysts and compromise catalytic activity as a result of loss in surface area.

In this work, we have shown highly active OER catalysts based on ZIF 67 which consists of Co as metal nodes and 2-

Received: April 15, 2019
Accepted: July 1, 2019
Published: July 1, 2019

Scheme 1. Synthesis of ZIF 67 Based Electrocatalysts

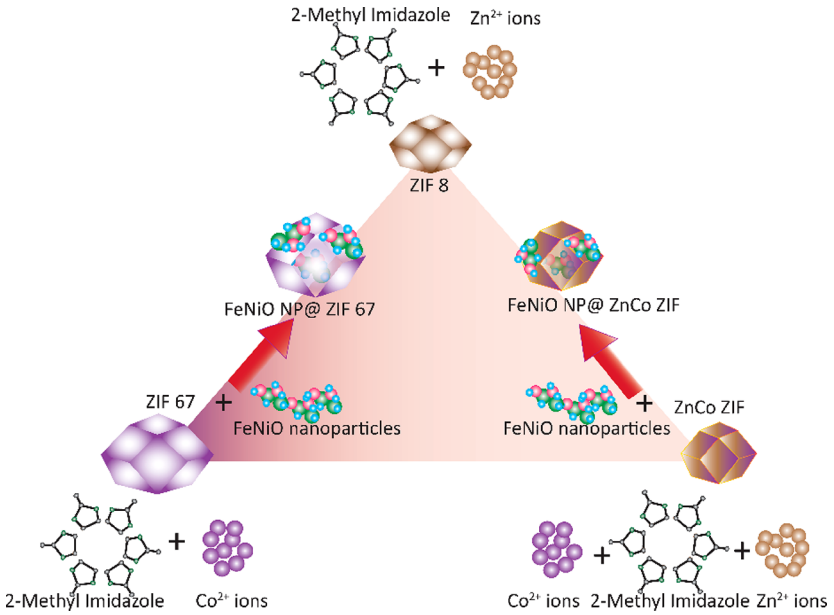

methylimidazole as the organic linker. The Co ions have a d^6/d^7 configuration that renders better orbital overlap with 2-methyl imidazole, which is beneficial for effective charge transfer.[29] In addition, Co itself exists as Co(II) and Co(III) which provides inherent charge transfer capability in ZIF 67.[30] For these two reasons, ZIF 67 is found to be 1000 times more conductive than ZIF 8, a commonly used Zn based MOF in catalysis, which, hence, negates the necessity of high temperature heat treatment to achieve suitable conductivity. Therefore, larger sized catalyst batches can be produced using unpyrolyzed ZIF 67. We demonstrate a new class of OER catalysts based on ZIF 67 with Fe, Ni, and Zn as dopants. Interestingly, none of these catalysts have been pyrolyzed due to the fundamental electronic advantage of ZIF 67. In our previous works, we have developed standardized experimental protocols to establish baselines in rotating disc electrode (RDE) and single-cell tests using standard, state of the art catalysts.[31] This work leverages previous efforts benchmarking catalyst activities and developing half- and single-cell test protocols for AEM electrolysis applications.

2. EXPERIMENTAL SECTION

2.1. Materials Synthesis. ZIF 67 was synthesized by dissolving 6.3 g of 2-methylimidazole in 100 mL of methanol. To this solution was added 2.9 g of cobalt nitrate hexahydrate ($Co(NO_3)_2{\cdot}6H_2O$), and a purple solution was obtained. The reaction mixture was stirred overnight under room temperature at 1000 rpm. The solid product was separated by centrifuging the reaction mixture at 3500 rpm. The product was purified by washing it in methanol and centrifuging it at 3500 rpm for 30 min. To ensure removal of contaminants, this step was repeated three times. ZnCo ZIF was synthesized using a method similar to that for ZIF 67, keeping the molar concentration of metals the same. In brief, 6.3 g of 2-methylimidazole was dissolved in 100 mL methanol. To this solution, 1.49 g of zinc nitrate ($Zn(NO_3)_2{\cdot}6H_2O$) and 1.46 g of cobalt nitrate ($Co(NO_3)_2{\cdot}6H_2O$) were added. A light purple colored solution was obtained which was stirred overnight at 1000 rpm under room temperature. The solid product was separated and purified by centrifugation. Composites of Fe_2O_3/NiO nanoparticles with ZIF 67 (denoted as FeNiO NP@ZIF 67) and ZnCo (denoted by FeNiO NP@ZnCo ZIF) were also synthesized to observe the resulting effect on OER catalysis. FeNiO NP@ZIF 67 composite was made by making a suspension of 50 mg of Fe_2O_3/NiO nanoparticles (Sigma-Aldrich, 50 nm) in methanol. To this were added 6.3 g of 2-methylimidazole and 2.9 g of cobalt nitrate hexahydrate. The reaction mixture was stirred overnight, and the solid product was collected the next day by centrifugation. The material was purified by the same technique as mentioned before. FeNiO NP@ZnCo ZIF composite was made by preparing a solution of FeNiO nanoparticles in 100 mL of methanol. To this suspension were added 6.3 g of 2-methylimidazole, 1.46 g of cobalt nitrate, and 1.49 g of zinc nitrate. The solution was stirred at 1000 rpm at room temperature overnight. The solid catalyst was then separated and purified by centrifugation. ZIF 8 was prepared using an aqueous route. An 11.12 g portion of 2-methylimidazole was dissolved in 100 mL of deionized water. To this solution was added 0.57 g of zinc nitrate hexahydrate, and a milky white suspension was obtained. The reaction was stirred overnight at room temperature, and the solid product was collected and purified by centrifugation. Scheme 1 illustrates the material synthesis procedure and the structures of the catalysts, summarizing the details mentioned above.

2.2. Physicochemical Characterization. XRD characterization was carried out using a Rigaku Ultima IV instrument with a Cu Kα source (λ = 1.541 Å) operated at 40 kV and 40 mA. $2\theta/\theta$ scans were collected using a step size of 0.02° and step duration of 5 s. Data refining, background correction, and phase identification were done using JADE 60 software.

2.2.1. Transmission Emission Microscopy (TEM) and Electron Dispersive Spectroscopy (EDS). TEM and EDS data were collected at 200 kV operating voltage using Philips CM200 and FEI Talos instruments where samples were dried on a copper grid with holey carbon films as support.

2.2.2. Brunauer–Emmett–Teller (BET). Surface areas of the ZIF based catalysts were obtained from the nitrogen physisorption adsorption isotherms measured using a Micromeritics ASAP 2020 instrument. All samples were degassed to 200 °C in vacuum to eliminate any surface water prior to measurement. The BET surface area was determined in general in the range 0.002–0.1 P/P_o, (where P_o is the measured saturation pressure of N_2).

2.2.3. Inductively Coupled Plasma Mass Spectrometry (ICP-MS). To assess the extent of catalyst dissolution during durability measurements, the electrolyte sample post durability was analyzed using ICP-MS without diluting. Three different concentrations (2, 20, and 200 ppb) of standard solutions using Co, Fe, Ni, and Zn were made in 0.1 M NaOH solution. The instrument was then calibrated to a blank internal standard and the Co, Fe, Ni, and Zn standards. Three

DOI: 10.1021/acsaem.9b00733
ACS Appl. Energy Mater. XXXX, XXX, XXX−XXX

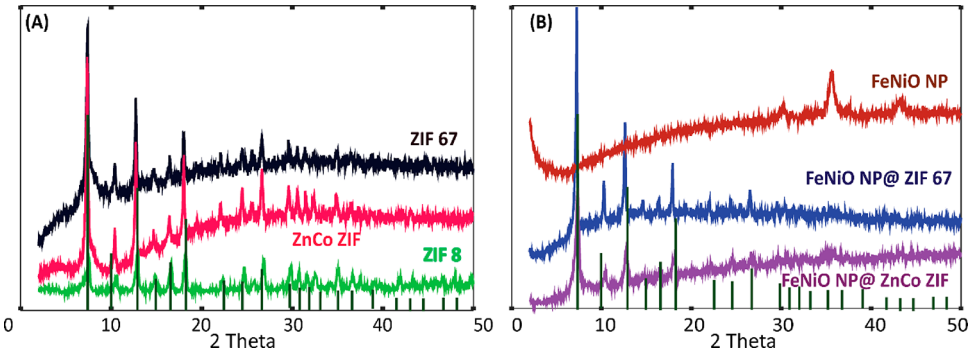

Figure 1. XRD diffraction pattern of (a) ZIF 8, ZIF 67, including ZnCo ZIF and nanoparticle/ZIF composites, and (b) FeNiO nanoparticles, FeNiO@ZIF 67, and FeNiO@ZnCo ZIF catalysts.

measurements were taken at each concentration using a dwell time of 0.15 s. To ensure proper calibration of the instrument during measurements, ICP-MS was checked to a Co standard after every 5 analyses.

2.2.4. X-ray Fluorescence (XRF). In order to confirm the metal loading on the electrodes, a Fisherscope XDV-SDD XRF spectrometer with a 50 kV, 50 W X-ray source was used. A minimum of three areas on each electrode were probed, and the final loading was determined by taking a mean value.

2.3. RDE Testing. The catalyst inks were made by adding 7 mg of catalysts in 3.8 mL of deionized water and 1.2 mL of isopropyl alcohol. The suspension was then kept in ice for 5 min following which 80 μL of 5% Nafion solution was added. The catalyst ink was then sonicated in ice cold water for 20 min with manual shaking of the ink every 5 min. A 10 μL portion of the as-prepared ink was then drop-casted on a gold RDE tip (5 mm diameter) by spin-coating to obtain 71 $\mu g/cm^2$ of the catalyst and 20 $\mu g/cm^2$ of cobalt loadings, respectively. Gold tips were used to avoid glassy carbon electrode corrosion and to ensure that durability losses were due to the catalyst and did not incorporate substrate corrosion and catalyst delamination during extended operation at elevated potential. While gold did not provide OER activity in the potential range of interest, it did participate in cyclic voltammograms, most noticeably in a cathodic peak at 1.1 V_{RHE} due to the reduction of gold oxide (Figure S1). Electrochemical tests were done using an Autolab (Ecochemie Inc. PGSTAT 30) potentiostat/galvanostat with an FRA 32 Module. All tests were done using a three electrode Teflon cell using 0.1 M NaOH (Traceselect, Sigma-Aldrich) as the electrolyte. A gold mesh was used as the counter electrode and Hg/HgO electrode was used a reference. Prior to any electrochemical test, the Hg/HgO reference electrode was calibrated from the potential at zero current in the HER/HOR region using a polycrystalline Pt electrode. All the electrochemical data shown in this report are presented in RHE potential scale by using individually calibrated results for Hg/HgO reference electrode. OER polarization data was collected at a 10 mV s^{-1} scan rate in N_2 saturated 0.1 M NaOH while rotating the working electrode at 2500 rpm (to eradicate any resistance by accumulation of gas bubbles), and cyclic voltammograms were collected at scan rates of 100, 50, and 10 mV s^{-1} scan rates. The electrochemical impedance spectroscopy (EIS) data was collected at 100 mV intervals from 1.4 V_{RHE} to 1.9 V_{RHE} using frequency ranges from 10 kHz to 100 mHz.

2.4. Membrane Electrode Assemble (MEA) Testing. The anode and cathode catalysts were sprayed on carbon Toray papers using the dry catalyst powder, Sustainion XB-7 ionomer, isopropanol, and water. A 5 cm^2 MEA was prepared using Sustainion membrane X37-50 pressed between a Pt cathode (0.1 mg/cm^2) and an anode with 0.6–0.8 mg/cm^2 active metal loading. Prior to testing, the X37-50 membrane was soaked in 1 M KOH for at least 24 h for converting the membrane from the chloride form to the hydroxide form. The choice of this commercially available membrane was based on the fact that this membrane generated higher currents at lower overpotentials for a given catalyst and was comparatively easier to handle. The cell hardware was obtained from Fuel Cell Technologies with aluminum end plates and nickel flow field. The electrolyte was circulated at the anode and cathode at a flow rate of 100 mL/min. The MEA was conditioned by holding the cell at a potential of 2 V for 1 h, or until a steady current response was obtained. The polarization curves were obtained under steady state conditions by holding the cell at desirable potentials for 120 s and acquiring the current output. Cyclic voltammograms were obtained at 100, 50, and 20 mV s^{-1} scan rates. EIS data was collected between 1.4 and 1.9 V using frequency ranges from 10 kHz to 1 Hz. All the data were collected at 60 and 80 °C. The high frequency resistance value was found to be 20 mΩ and was used to evaluate the *iR*-free voltage.

3. RESULTS AND DISCUSSION

Figure 1a shows the XRD diffraction pattern for ZIF 67, ZnCo ZIF, and ZIF 8. The obtained patterns were in accordance with the simulated sodalite diffraction pattern reported in the literature, establishing the successful formation of the ZIF structure.[32−34] XRD diffraction patterns of FeNiO nanoparticles, an FeNiO nanoparticle composite with ZIF 67 (FeNiO NP@ZIF 67), and an FeNiO nanoparticle composite with ZnCo ZIF (FeNiO NP@ZnCo ZIF) are displayed in Figure 1b. While a pair of sharp peaks corresponding to NiO(111) at 2θ = 37° and α-Fe_2O_3(440) at 2θ = 45° were identified in the XRD data to be from bare FeNiO nanoparticles, these peaks disappeared when conjugated with the ZIF 67 and ZnCo ZIF. This was likely due to the fact that the weight percentage of the FeNiO nanoparticles was small (Fe ∼ 1 wt %, Ni ∼ 0.6 wt %, and Co ∼ 18 wt % from EDS analysis) in comparison to the ZIFs, and the representative diffraction peaks of Fe and Ni may have been shielded. Alternatively, a partial or complete encapsulation of the FeNiO nanoparticles by the ZIFs may also have caused the disappearance of the diffraction peaks of the FeNiO NP@ZIF 67 and FeNiO NP@ZnCo ZIFs catalysts.[35]

High resolution TEM images of ZIF 67 crystals confirmed that the crystals were homogeneous and monodispersed, with a uniform crystal size of ∼450 nm (Figure 2A,B). EDS mapping was completed for Co and O distribution within the ZIF 67 catalyst (Figure 2C). The surface of the ZIF 67 nanoparticles was found to be passivated with an oxide layer, as seen in the TEM image. This trait can be expected since Co is highly oxophilic and hence tends to oxidize under ambient conditions. High resolution TEM images of ZIF 8 nanoparticles showed a spherical/hexagonal shape with a smaller particle size of ∼200 nm (Figure 2D−F). As depicted in the overlay image (Figure 2F), Zn is homogeneously distributed throughout the particles, while there is a slightly higher concentration of oxygen along the edges. ZnCo particles were

DOI: 10.1021/acsaem.9b00733
ACS Appl. Energy Mater. XXXX, XXX, XXX−XXX

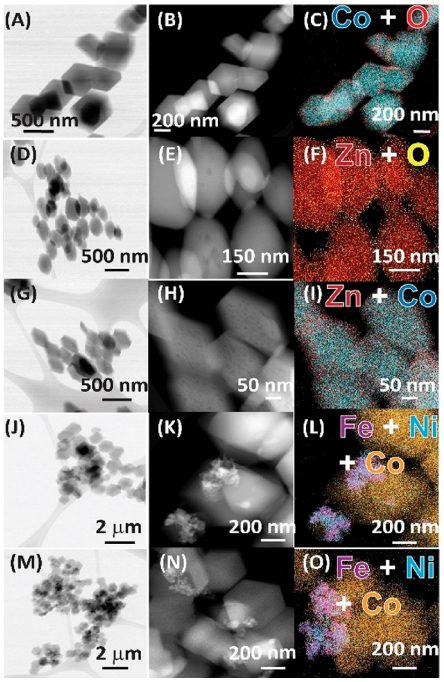

Figure 2. TEM and EDS mapping of ZIF 67 (A–C), ZIF 8 (D–F), ZnCo ZIF (G–I), FeNiO NP@ZIF 67 (J–L), and FeNiO NP@ZnCo ZIF. Left panel corresponds to bright field images at low magnification. Middle panel shows dark field images collected at high magnification. Right panel displays the elemental mapping in each catalyst at high magnification.

~250 nm in size (similar size to ZIF 8) but shaped as oblong hexagons that resembled the morphology of ZIF 67 (Figure 2G–I). EDS elemental analysis revealed that Co and Zn exist in an atomic ratio of 1.4. The ZnCo particles appeared to have a porous structure which was not detected prominently for ZIF 8 or ZIF 67. As reported by Yu et al.,[36] the presence of Zn precursors results in a greater distance between two Co nodes, which may cause the porous framework of ZnCo ZIF. From the TEM images, it seemed that features of ZIF 67 and ZIF 8 were combined during ZnCo ZIF synthesis, resulting in a homogeneous framework consisting of Zn and Co as metallic nodes. An interesting feature was the absence of a passivating oxide layer on the ZnCo particles (Figure S2), likely due to the presence of Zn. Zn preventing Co surface passivation may have played a role in improving catalyst durability during electrochemical testing, which has been discussed in later sections. For FeNiO NP@ZIF 67 and FeNiO NP@ZnCo ZIF, the FeNiO nanoparticles were segregated into one region while the Ni was evenly distributed across the entire ZIF (Figure 2J–O and Figure S3). Elemental analysis was carried out in both low and high magnification modes, demonstrating consistency in elemental composition (except for Fe distribution in FeNiO NP@ZIF 67 and FeNiO NP@ZnCo catalysts) and homogeneity throughout the particles.

The ZIF 67 based catalysts evaluated had high BET surface areas, as reported in Table 1. While ZIF 67 had a surface area of 1610 m^2/g, ZnCo ZIF had a surface area of 1760 m^2/g; this was expected since Zn is known to induce porosity[36] and is shown via microscopy (Figure 2H). The commercially available FeNiO nanoparticles had lower surface area of 180 m^2/g. As these nanoparticles were conjugated with ZIF 67 and ZnCo ZIF, the surface areas of the resulting composites

Table 1. Comparison between BET Surface Area and Double Layer Capacitance (Normalized to the Geometric Area) of the ZIF Based Catalysts

catalyst	surface area	C_{dl}
FeNiO nanoparticles	180 m^2/g	
ZIF 67	1610 m^2/g	336 $\mu F\ cm^{-2}$
ZnCo ZIF	1760 m^2/g	433 $\mu F\ cm^{-2}$
FeNiO NP@ZIF 67	1190 m^2/g	204 $\mu F\ cm^{-2}$
FeNiO NP@ZnCo ZIF	1390 m^2/g	255 $\mu F\ cm^{-2}$

decreased by over 25% compared to the surface area of the original ZIFs. This can be a result of the nanoparticles residing on the surface or subsurface of ZIFs, thereby blocking some pores which become inaccessible for gas adsorption. This may also be an effect of the low surface area FeNiO nanoparticles that reduce the net BET surface area of the ZIF based conjugates. The double layer capacitance of the ZIF based catalysts was evaluated as they are indicative of the electrochemical active surface area (ECSA) for the precious metal free catalysts.[37] The trends of BET areas and electrochemically active areas seem to match where ZnCo ZIF was found to have the highest value while FeNiO NP@ZIF 67 was found to have the lowest values of ECSA. This is interesting considering the fact that ECSA is not related to BET in general, as BET accounts for a nonelectroactive surface area as well. This observation indicates the electrochemical activities of the catalysts are heavily influenced by their porosity and BET surface areas.

Figure 3A shows the cyclic voltammograms of ZIF based catalysts collected in N_2 purged 0.1 M NaOH electrolyte. The presence of multiple Co oxidation states was evident from the oxidation peaks appearing in the cyclic voltammograms. The anodic peak at 1.08 V_{RHE} corresponds to the transformation of Co^{2+}/Co^{3+}, whereas the oxidation peak at 1.3 V_{RHE} is due to the Co^{3+}/Co^{4+} redox transition. The Co^{3+}/Co^{4+} transition appears to be much earlier and stronger in ZIF 67 and FeNiO NP@ZIF 67 catalysts compared to the other two catalysts that contain Zn. The presence of Zn clearly subdued the transition of Co^{3+}/Co^{4+} as the peaks were shifted to a higher potential and had a lower intensity in the case of the ZnCo ZIF and FeNiO NP@ZnCo ZIF catalysts. This can be explained as an inductive effect, where Zn increased the covalent character of the Co–O–Co bond and raised the electron energy of the valence band.[38] This result may also be correlated to the EDS results where the elemental analysis showed the absence of a passivating oxide layer on the outer surfaces of ZnCo ZIF and FeNiO NP@ZnCo ZIF particles, indicating that Zn may prevent the oxidation of Co centers. The strong anodic peak at 1.5 V_{RHE} observed in all the catalysts was the result of water oxidation. The OER polarization curves of the different ZIF 67 based catalysts alongside state of the art iridium oxide catalyst are plotted in Figure 3B. Iridium oxide catalyst showed the lowest onset potential at 1.57 V_{RHE}, closely followed by ZIF 67 for which the OER onset potential is 1.58 V_{RHE}. The rest of the ZIF based catalysts, e.g., ZnCo ZIF and FeNiO NP@ZnCo ZIF catalysts, exhibit OER onset around 1.64 V_{RHE}.

OER electrocatalysts were evaluated by comparing their overpotential losses at 10 mA/cm^2 current density, since 10 mA/cm^2 is the current density expected at the anode of a 10% efficient solar energy driven water splitting cell operating at 1 sun illumination.[39] Following this benchmark, ZIF 67 showed the highest efficiency with an overpotential of 420 mV at a

DOI: 10.1021/acsaem.9b00733
ACS Appl. Energy Mater. XXXX, XXX, XXX−XXX

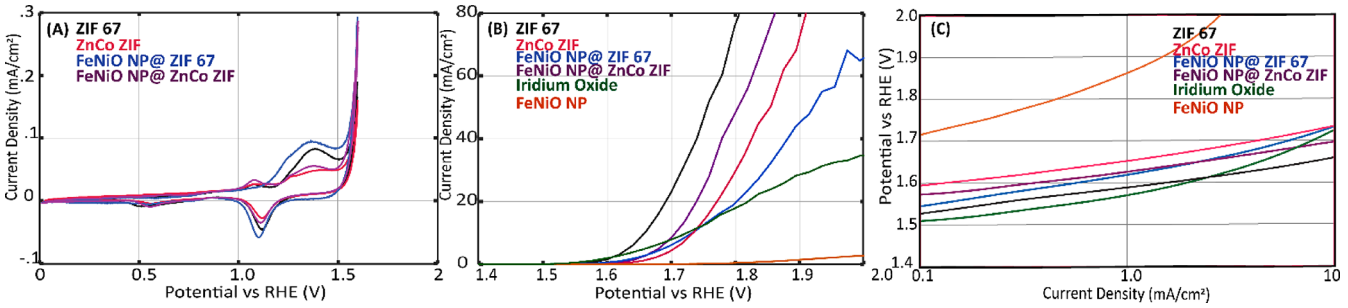

Figure 3. Cyclic voltammogram (A), OER polarization curves (B), and Tafel plots (C) of ZIF 67 based electrocatalysts collected in N_2 purged 0.1 M NaOH at a scan rate of 10 mV s^{-1}.

Table 2. Summary of OER Performance of the ZIF Based Catalysts Obtained from RDE Experiments in N_2 Saturated 0.1 M NaOH Electrolyte Collected at a Scan Rate of 10 mV s^{-1}

catalyst	OER onset potential	potential at 10 mA/cm^2	Tafel slope	charge transfer resistance at 1.7 V_{RHE}
ZIF 67	1.58 V	1.65 V	78 mV/dec	101 Ω
ZnCo ZIF	1.78 V	1.74 V	86 mV/dec	170 Ω
FeNiO NP@ZIF 67	1.63 V	1.73 V	120 mV/dec	100 Ω
FeNiO NP@ZnCo ZIF	1.63 V	1.69 V	82 mV/dec	90 Ω

current density of 10 mA/cm^2 and iridium oxide suffered from a higher overpotential loss (500 mV) at the same current density. Though iridium oxide had the lowest OER onset potential, the Ir surface gets heavily passivated at higher potentials that leads to such loss in activity.[40] The corresponding Tafel plots presented in Figure 3C provide a better perspective on the activities of these catalysts. In the kinetically controlled low current region, iridium oxide shows a higher activity than the ZIF based catalysts. ZIF 67 closely follows the activity of iridium oxide in the kinetic region but surpasses the state of the art catalyst at high current densities. The high surface area and efficient management of gas bubbles imparted by the porous framework help to reduce the mass transport losses in ZIF 67, escalating its performance over iridium oxide especially at high current densities. This trend is also manifested in the MEA performance, which is discussed in later sections. Compared to that for ZIF 67 which has a lower onset potential, the OER onset in ZnCo ZIF occurs at 1.78 V_{RHE}. The presence of Zn blocked the Co active sites, resulting in an inferior performance by reducing the number of available active sites as well as interfering with the intrinsic catalytic activity of the Co centers. FeNiO NP@ZnCo ZIF and FeNiO NP@ZIF 67 catalysts showed similar activities with an onset potential of 1.63 V_{RHE}. However, when the bare FeNiO nanoparticles were tested for their OER activity, the OER onset (1.85 V_{RHE}) and overpotential at 10 mA/cm^2 were extremely high, owing to their very low surface area and large particle sizes. This observation indicated that the OER activities in the composite catalysts were not influenced by the Fe_2O_3/NiO nanoparticles (contrary to the usual expectations that Fe and Ni metals enhance OER activity). A look at the Tafel plots and Tafel slope values (Figure 3C, Table 2) revealed that, among the given catalysts, ZIF 67 had the lowest value of Tafel slope of 78 mV/dec, followed by FeNiO NP@ZnCo ZIF and ZnCo ZIF with a Tafel slope of ~86 mV/dec, and FeNiO NP@ZIF 67 with the highest value of 120 mV/dec. This trend may imply that the presence of Fe_2O_3/NiO nanoparticles obstructed OH^- adsorption on the catalyst surface, potentially making this step rate limiting. However, if Zn was also present in the system, a Fe/Ni/Zn synergistic effect may occur that aids in faster OH^- adsorption, supported by the lower FeNiO NP@ZnCo ZIF and ZnCo ZIF Tafel slope. Zinc is known to increase the electrophilicity of Co sites that aids in faster adsorption of OH^- ions, as observed previously,[41] and, hence, may explain the observed decrease in the Tafel slope in the case of FeNiO NP@ZnCo ZIF. A similar trend in Tafel slope was also observed by Zhou et al. where addition of Zn in nickel based hydroxides resulted in the lowering of Tafel slope compared to that of bare Ni hydroxide nanoarrays.[42] These results indicated that Co atoms were the sole active sites in these catalysts and inclusion of nanoparticles caused a decrease in OER activity by impairing OH^- adsorption. All the ZIF based catalysts were tested to evaluate their charge transfer resistance (CTR) values using EIS and are reported in Table 2, and the corresponding Nyquist plots are presented in Figure S4. The ohmic resistance in all the catalysts (irrespective of applied potential) had a steady value of 40 Ω. Such a consistent value of high frequency resistance (HFR) from EIS is expected since in the RDE setup this value corresponds to the electrolyte resistance sensed between the working electrode and the reference electrode. While both ZIF 67 and FeNiO@ZIF 67 had very similar charge transfer resistance (CTR) values of ~100 Ω (measured at 1.7 V_{RHE}), ZnCo ZIF had a considerably higher value (170 Ω). The high CTR for ZnCo is a result of Zn moieties in the framework since they lack electronic conductivity (as a result of d^{10} electronic configuration of Zn(II) and poor orbital overlap between Zn and 2-methylimidazole ligands). The composite FeNiO@ZnCo catalyst had the lowest CTR of 90 Ω, indicating that the Fe_2O_3/NiO nanoparticles aided in lowering the high charge transfer resistance of ZnCo ZIF. Though the exact mechanism of this effect is unknown, it may be a result of modified charge distribution among Fe, Ni, Co, and Zn in the catalyst framework.[43] From the EDS mapping results, Ni was found to be evenly distributed throughout the catalyst unlike Fe. This phenomenon may have played a role in decreasing the charge transfer resistance of FeNiO NP@ZnCo ZIF compared to ZnCo ZIF. This observation in conjunction with the low CTR value of FeNiO NP@ZIF 67 suggested that, despite the nanoparticles being partially located on surface or subsurface of

DOI: 10.1021/acsaem.9b00733
ACS Appl. Energy Mater. XXXX, XXX, XXX−XXX

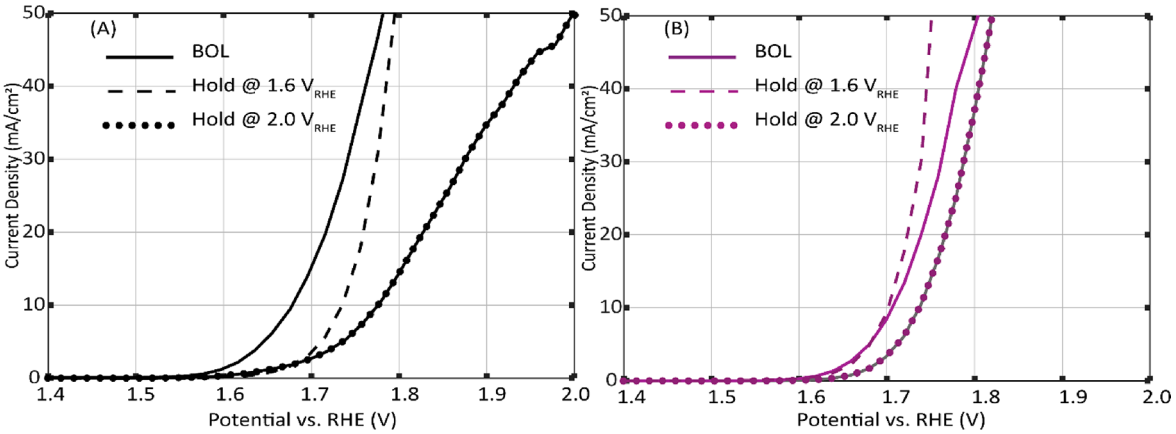

Figure 4. OER polarization curves of ZIF based catalysts at BOL and after being held at 1.6 V_{RHE} and 2.0 V_{RHE} for ZIF 67 (A) and FeNiO NP@ZnCo ZIF (B). Data were collected in N_2 purged 0.1 M NaOH at 10 mV s^{-1} scan rates.

the ZIFs, they did not hinder the charge transfer process occurring at the electrode/electrolyte interface.

The reported catalysts were tested for durability by holding at 1.6 V_{RHE} since the losses are similar to those encountered in MEA at the same potential (for a shorter period of time).[44] To study the effect of exposure to a higher potential, the working electrode was held at 2.0 V. Considering the high operating potential of electrolyzers, the metals are expected to be in their oxidized form. The OER polarization curves for ZIF 67 and FeNiO NP@ZnCo ZIF measured at the beginning of life (BOL) and after potential holds at 1.6 V_{RHE} and 2.0 V_{RHE} are shown in Figure 4A,B. The collective results from the durability experiments for all the catalysts are summarized in Table 3. The OER polarization data of ZIF 67 post durability measurement showed significant losses when comparing the overpotential at 10 mA/cm^2. Surprisingly, both ZnCo ZIF and FeNiO NP@ZnCo ZIF underwent minimal losses compared to the other two catalysts. Like ZIF 67, the FeNiO NP@ZIF 67 catalyst also has higher overpotential loss (post durability) at 10 mA/cm^2 current density. ICP analyses of the electrolyte samples (Table S1) post durability revealed that minimal metal dissolution occurred during the experiment, and hence, the observed losses in the OER activity may have been due to passivation of the catalyst surface. The OER activity losses summarized in Table 3 indicate that catalysts containing Zn (ZnCo ZIF and FeNiO NP@ZnCo ZIF) suffered fewer activity losses compared to the catalysts without Zn. Hence it seems that the presence of Zn in the catalyst helped retain the catalytic activity by protecting the active sites from passivation. We observed a similar trend for ex situ TEM analysis (Figure S2) where the catalysts with Zn as a component (ZnCo ZIF and FeNiO@ZnCo ZIF) did not have an outer oxide layer on their surface. This effect was also demonstrated by Rong et.al.,[45] where they found that the presence of Zn helped retain the activity of the Co center by preventing the formation of higher oxidation states of Co. Although due to experimental limitations the exact contribution of each of the participating metals (Co, Fe, Zn, Fe, and Ni) toward OER cannot be determined, evidence points to Co being the sole active site in these catalysts with Zn aiding in increasing the stability of the

Table 3. Summary of Durability Analysis of the ZIF Based Catalysts toward OER Obtained from RDE Experiments in N_2 Saturated 0.1 M NaOH Electrolyte[a]

	potential at 10 mA/cm^2		
catalyst	BOL	1.6 V_{RHE}	2.0 V_{RHE}
ZIF 67	1.65 V	1.73 V	1.78 V
ZnCo ZIF	1.73 V	1.70 V	1.73 V
FeNiO NP@ZIF 67	1.69 V	1.73 V	1.77 V
FeNiO NP@ZnCo ZIF	1.70 V	1.70 V	1.73 V

[a]Data was collected at a sweep rate of 10 mV s^{-1}.

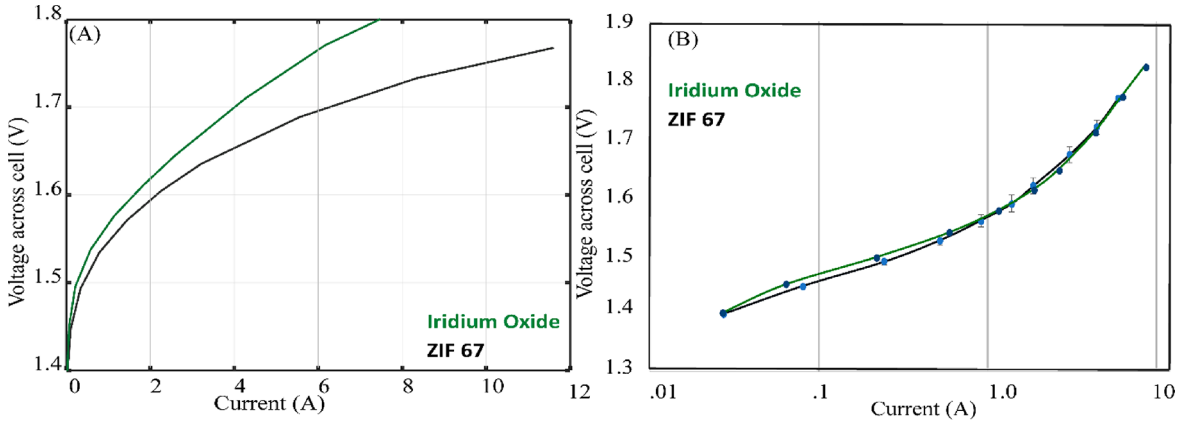

Figure 5. (A) *iR* corrected steady state polarization curves obtained with 1 M KOH (at cathode and anode) with 5 cm^2 electrode in an electrolyzer cell operated at 60 °C. (B) Tafel plots of ZIF 67 and iridium oxide catalysts obtained from the steady state polarization curves.

DOI: 10.1021/acsaem.9b00733
ACS Appl. Energy Mater. XXXX, XXX, XXX−XXX

catalysts by preventing passivation. FeNiO nanoparticles did not enhance OER but impeded OH^- adsorption due to their site-blocking effect, though this effect should be considered as a consequence of the structure of the FeNiO NP@ZIF 67 and FeNiO NP@ZnCo ZIF catalysts where large sized FeNiO nanoparticles were blocking the Co active sites. Other systems where Fe and Ni ions can be incorporated homogeneously into ZIF structures need to be studied in order to understand the role of Fe and Ni toward OER in non-heat-treated ZIF 67 and ZnCo ZIF catalysts. A comparison of recently reported catalysts that have used ZIF 67 as a component or template has been presented in Table S3. In addition to exhibiting comparable activities to the other reported catalysts, ZIF 67 has an added advantage in terms of scalability that is important for establishing it as anodes in AEM water electrolyzers.

Among the ZIF 67 based catalysts, the best performing ZIF 67 was selected for assessing the MEA performance. It should be noted that no durability experiments were performed in the single cells and hence the choice of catalyst was based solely on their activity in RDE experiments. ZIF 67 was spray coated on 5 cm^2 5% PTFE wet proofed carbon Toray paper and was used as the anode in an electrolyzer cell operated at 60 °C using 1 M KOH. The loadings of active metal Co in the anodes were maintained around 0.6−0.8 mg/cm^2, whereas a Pt/C electrode with a metal loading of 0.1 mg/cm^2 was used as the cathode. Steady state polarization data were collected, and the resulting curves are plotted in Figure 5A. A state of the art catalyst for OER, iridium oxide, was tested as a reference and is included in the plot. Comparing the current generated at an operating voltage of 1.6 $V_{iR\text{-free}}$, ZIF 67 exhibited a higher performance of 2.3 A, surpassing iridium oxide (1.8 A). *iR* corrected Tafel plots in Figure 5B were used to compare catalysts in the kinetic region, where ZIF 67 and iridium oxide produced similar performances. Therefore, the enhanced performance of ZIF 67 compared to iridium oxide was likely an effect of the higher porosity of ZIF 67 mitigating transport losses at higher currents. Nevertheless, it is important to note that the ZIF 67 catalyst outperformed the state of the art iridium oxide by a significant margin, therefore presenting a promising future as anodes in AEM electrolyzers.

4. CONCLUSION

In this report, we have successfully demonstrated OER activity by untreated ZIF 67 based catalysts. These catalysts consisted of Co and Zn as metal anodes and Fe, Ni, and dopants. These catalysts were prepared by simple wet chemical methods and have been used as-synthesized, without any heat treatment, thereby increasing the yield of active catalyst by avoiding the mass loss usually encountered during pyrolysis. Various factors interplay as a result of combining the different transition metals present in the catalyst framework. While addition of Zn was found to be beneficial toward lowering the Tafel slope and reducing activity losses due to passivation during extended operation, the presence of Zn also resulted in very high charge transfer resistance. On the other hand, the inclusion of Fe_2O_3/NiO nanoparticles was found to be detrimental toward OER activity by slowing down OH^- adsorption rate, likely due to a site-blocking effect. These nanoparticles, however, significantly reduced the charge transfer resistance imparted by Zn in FeNiO NP@ZnCo ZIF. Other synthesis routes may be explored to ensure better distribution of Fe and Ni atoms in the ZIF structure that may impact OER activity in a different way than observed here. In this work, bare ZIF 67 was found to be the most active both in RDE and MEA tests. In the future, the durability data under MEA testing conditions will be tested using ZIF 67 based catalysts in order to establish these catalysts as commercial anodes in the power market.

■ ASSOCIATED CONTENT

Supporting Information

The Supporting Information is available free of charge on the ACS Publications website at DOI: 10.1021/acsaem.9b00733.

Supplementary data on XRD, RDE, and EDS elemental mapping (PDF)

■ AUTHOR INFORMATION

Corresponding Author

*E-mail: Shaun.Alia@nrel.gov. Phone: 303-275-3748. Fax: 303-275-3840.

ORCID

Svitlana Pylypenko: 0000-0001-7982-734X

Shaun M. Alia: 0000-0002-7647-9383

Notes

The authors declare no competing financial interest.

■ ACKNOWLEDGMENTS

This work was supported by the Laboratory Directed Research and Development (LDRD) Program at the National Renewable Energy Laboratory. NREL is a national laboratory of the U.S. Department of Energy, Office of Energy Efficiency and Renewable Energy, operated by the Alliance for Sustainable Energy, LLC. This work was authored in part by the National Renewable Energy Laboratory, operated by Alliance for Sustainable Energy, LLC, for the U.S. Department of Energy (DOE) under Contract No. DE-AC36-08GO28308. Funding was provided by the U.S. Department of Energy Office of Energy Efficiency and Renewable Energy Fuel Cell Technologies Office. The views expressed in the article do not necessarily represent the views of the DOE or the U.S. Government. The U.S. Government retains and the publisher, by accepting the article for publication, acknowledges that the U.S. Government retains a nonexclusive, paid-up, irrevocable, worldwide license to publish or reproduce the published form of this work, or allow others to do so, for U.S. Government purposes.

■ REFERENCES

(1) Staffell, I.; Scamman, D.; Velazquez Abad, A.; Balcombe, P.; Dodds, P. E.; Ekins, P.; Shah, N.; Ward, K. R. The role of hydrogen and fuel cells in the global energy system Energy. *Energy Environ. Sci.* **2019**, *12*, 463−491.

(2) Pivovar, B.; Rustagi, N.; Satyapal, S. Hydrogen at Scale (H2 @ Scale) Key to a Clean, Economic, and Sustainable Energy System. *Electrochem. Soc. Interface* **2018**, *27*, 47−52.

(3) Vickers, J. W.; Dinh, H. N.; Randolph, K.; Weber, A. Z.; McDaniel, A. H.; Boardman, R.; Ogitsu, T.; Colon-Mercado, H.; Peterson, D.; Miller, E. L. HydroGEN: An AWSM Energy Materials Network. *ECS Trans.* **2018**, *85*, 3−14.

(4) Suntivich, J.; May, K. J.; Gasteiger, H. A.; Goodenough, J. B.; Shao-Horn, Y. A Perovskite Oxide Optimized for Oxygen Evolution Catalysis from Molecular Orbital Principles. *Science* **2011**, *334*, 1383−1385.

(5) Alia, S. M.; Shulda, S.; Ngo, C.; Pylypenko, S.; Pivovar, B. S. Iridium-Based Nanowires as Highly Active, Oxygen Evolution Reaction Electrocatalysts. *ACS Catal.* **2018**, *8*, 2111−2120.

DOI: 10.1021/acsaem.9b00733
ACS Appl. Energy Mater. XXXX, XXX, XXX−XXX

(6) Gorlin, Y.; Jaramillo, T. F. A Bifunctional Nonprecious Metal Catalyst for Oxygen Reduction and Water Oxidation. *J. Am. Chem. Soc.* **2010**, *132*, 13612−13614.
(7) Deng, J.; Ren, P.; Deng, D.; Yu, L.; Yang, F.; Bao, X. Highly Active and Durable Non-Precious-Metal Catalysts Encapsulated in Carbon Nanotubes for Hydrogen Evolution Reaction Energy. *Energy Environ. Sci.* **2014**, *7*, 1919−1923.
(8) Zeng, Y.; Chen, L.; Chen, R.; Wang, Y.; Xie, C.; Tao, L.; Huang, L.; Wang, S. One-step, room temperature generation of porous and amorphous cobalt hydroxysulfides from layered double hydroxides for superior oxygen evolution reactions. *J. Mater. Chem. A* **2018**, *6*, 24311−24316.
(9) Landon, J.; Demeter, E.; Inoglu, N.; Keturakis, C.; Wachs, I. E.; Vasic, R.; Frenkel, A. I.; Kitchin, J. R. Spectroscopic Characterization of Mixed Fe−Ni Oxide Electrocatalysts for the Oxygen Evolution Reaction in Alkaline Electrolytes. *ACS Catal.* **2012**, *2*, 1793−1801.
(10) Burke, M. S.; Enman, L. J.; Batchellor, A. S.; Zou, S.; Boettcher, S. W. Oxygen Evolution Reaction Electrocatalysis on Transition Metal Oxides and (Oxy)hydroxides: Activity Trends and Design Principles. *Chem. Mater.* **2015**, *27*, 7549−7558.
(11) Bates, M. K.; Jia, Q.; Doan, H.; Liang, W.; Mukerjee, S. Charge-Transfer Effects in Ni−Fe and Ni−Fe−Co Mixed-Metal Oxides for the Alkaline Oxygen Evolution Reaction. *ACS Catal.* **2016**, *6*, 155−161.
(12) Maiyalagan, T.; Jarvis, K. A.; Therese, S.; Ferreira, P. J.; Manthiram, A. Spinel-Type Lithium Cobalt Oxide as a Bifunctional Electrocatalyst for the Oxygen Evolution and Oxygen Reduction Reactions. *Nat. Commun.* **2014**, *5*, 3949−3956.
(13) Jin, C.; Lu, F.; Cao, X.; Yang, Z.; Yang, R. Facile Synthesis and Excellent Electrochemical Properties of NiCo2O4 Spinel Nanowire Arrays as a Bifunctional Catalyst for the Oxygen Reduction and Evolution Reaction. *J. Mater. Chem. A* **2013**, *1*, 12170−12177.
(14) Cheng, F.; Shen, J.; Peng, B.; Pan, Y.; Tao, Z.; Chen, J. Rapid Room-Temperature Synthesis of Nanocrystalline Spinels as Oxygen Reduction and Evolution Electrocatalysts. *Nat. Chem.* **2011**, *3*, 79−84.
(15) Xu, L.; Jiang, Q.; Xiao, Z.; Li, X.; Huo, J.; Wang, S.; Dai, L. Plasma-Engraved Co3 O4 Nanosheets with Oxygen Vacancies and High Surface Area for the Oxygen Evolution Reaction. *Angew. Chem., Int. Ed.* **2016**, *55*, 5277−5281.
(16) Li, X.; Wei, J.; Li, Q.; Zheng, S.; Xu, Y.; Du, P.; Chen, C.; Zhao, J.; Xue, H.; Xu, Q.; Pang, H. Nitrogen-Doped Cobalt Oxide Nanostructures Derived from Cobalt−Alanine Complexes for High-Performance Oxygen Evolution Reactions. *Adv. Funct. Mater.* **2018**, *28* (1−7), 1800886.
(17) Kim, J.; Yin, X.; Tsao, K.-C.; Fang, S.; Yang, H. Ca2Mn2O5 as Oxygen-Deficient Perovskite Electrocatalyst for Oxygen Evolution Reaction. *J. Am. Chem. Soc.* **2014**, *136*, 14646−14649.
(18) Bockris, J. O. M.; Otagawa, T. Mechanism of oxygen evolution on perovskites. *J. Phys. Chem.* **1983**, *87*, 2960−2971.
(19) Ma, T. Y.; Dai, S.; Jaroniec, M.; Qiao, S. Z. Metal−Organic Framework Derived Hybrid Co3O4-Carbon Porous Nanowire Arrays as Reversible Oxygen Evolution Electrodes. *J. Am. Chem. Soc.* **2014**, *136*, 13925−13931.
(20) Zhang, W.; Wu, Z.-Y.; Jiang, H.-L.; Yu, S.-H. Nanowire-Directed Templating Synthesis of Metal−Organic Framework Nanofibers and Their Derived Porous Doped Carbon Nanofibers for Enhanced Electrocatalysis. *J. Am. Chem. Soc.* **2014**, *136*, 14385−14388.
(21) Furukawa, H.; Cordova, K. E.; O'Keeffe, M.; Yaghi, O. M. The Chemistry and Applications of Metal-Organic Frameworks. *Science* **2013**, *341* (1−12), 1230444.
(22) Zheng, S.; Li, X.; Yan, B.; Hu, Q.; Xu, Y.; Xiao, X.; Xue, H.; Pang, H. Transition-metal (Fe, Co, Ni) based metal-organic frameworks for electrochemical energy storage. *Adv. Energy Mater.* **2017**, *7* (1−27), 1602733.
(23) Jiao, L.; Zhou, Y.-X.; Jiang, H.-L. Metal−Organic Framework-Based CoP/Reduced Graphene Oxide: High-Performance Bifunctional Electrocatalyst for Overall Water Splitting. *Chem. Sci.* **2016**, *7*, 1690−1695.
(24) Li, J.; Ghoshal, S.; Liang, W.; Sougrati, M.-T.; Jaouen, F.; Halevi, B.; McKinney, S.; McCool, G.; Ma, C.; Yuan, X.; Ma, Z. F.; Mukerjee, S.; Jia, Q. Structural and Mechanistic Basis for the High Activity of Fe−N−C Catalysts toward Oxygen Reduction Energy. *Energy Environ. Sci.* **2016**, *9*, 2418−2432.
(25) He, P.; Yu, X. Y.; Lou, X. W. D. Carbon-Incorporated Nickel−Cobalt Mixed Metal Phosphide Nanoboxes with Enhanced Electrocatalytic Activity for Oxygen Evolution. *Angew. Chem., Int. Ed.* **2017**, *56*, 3897−3900.
(26) Li, X.; Niu, Z.; Jiang, J.; Ai, L. Cobalt Nanoparticles Embedded in Porous N-rich Carbon as an Efficient Bifunctional Electrocatalyst for Water Splitting. *J. Mater. Chem. A* **2016**, *4*, 3204−3209.
(27) Jaouen, F.; Lefevre, M.; Dodelet, J.-P.; Cai, M. Heat-Treated Fe/N/C Catalysts for O2 Electroreduction: Are Active Sites Hosted in Micropores? *J. Phys. Chem. B* **2006**, *110*, 5553−5558.
(28) Wu, G.; More, K. L.; Johnston, C. M.; Zelenay, P. High-Performance Electrocatalysts for Oxygen Reduction Derived from Polyaniline, Iron, and Cobalt. *Science* **2011**, *332*, 443−447.
(29) Zhou, K.; Mousavi, B.; Luo, Z.; Phatanasri, S.; Chaemchuen, S.; Verpoort, F. A. Characterization and properties of Zn/Co zeolitic imidazolate frameworks vs. ZIF-8 and ZIF-67. *J. Mater. Chem. A* **2017**, *5*, 952−957.
(30) Butler, K. T.; Worrall, S. D.; Molloy, C. D.; Hendon, C. H.; Attfield, M. P.; Dryfe, R. A.; Walsh, A. Electronic Structure Design for Nanoporous, Electrically Conductive Zeolitic Imidazolate Frameworks. *J. Mater. Chem. C* **2017**, *5*, 7726−7731.
(31) Alia, S. M.; Pivovar, B. S. Evaluating Hydrogen Evolution and Oxidation in Alkaline Media to Establish Baselines. *J. Electrochem. Soc.* **2018**, *165*, F441−F445.
(32) Yang, J.; Zhang, F.; Lu, H.; Hong, X.; Jiang, H.; Wu, Y.; Li, Y. Hollow Zn/Co ZIF Particles Derived from Core−Shell ZIF-67@ZIF-8 as Selective Catalyst for the Semi-Hydrogenation of Acetylene. *Angew. Chem.* **2015**, *127*, 11039−11043.
(33) Qian, J.; Sun, F.; Qin, L. Hydrothermal Synthesis of Zeolitic Imidazolate Framework-67 (ZIF-67) Nanocrystals. *Mater. Lett.* **2012**, *82*, 220−223.
(34) Gross, A. F.; Sherman, E.; Vajo, J. J. Aqueous Room Temperature Synthesis of Cobalt and Zinc Sodalite Zeolitic Imidizolate Frameworks Dalton. *Trans.* **2012**, *41*, 5458−5460.
(35) Guo, X.; Deng, Y.; Gu, D.; Che, R.; Zhao, D. Synthesis and Microwave Absorption of Uniform Hematite Nanoparticles and their Core-Shell Mesoporous Silica Nanocomposites. *J. Mater. Chem.* **2009**, *19*, 6706−6712.
(36) Yu, W.; Liu, C.; Qiu, L.; Zhang, P.; Ma, W.; Yue, Y.; Xie, H.; Larkin, L. S. Advanced Thermal Interface Materials for Thermal Management. *Eng. Sci.* **2018**, *2*, 95−97.
(37) Han, H.; Choi, H.; Mhin, S.; Hong, Y.-R.; Kim, K. M.; Kwon, J.; Ali, G.; Chung, K. Y.; Je, M.; Umh, H. N.; Lim, D.-H.; Davey, K.; Qiao, S.-Z.; Paik, U.; Song, T. Advantageous Crystalline-Amorphous Phase Boundary for Enhanced Electrochemical Water Oxidation Energy *Energy Environ. Sci.* **2019**. DOI: 10.1039/C9EE00950G
(38) Kuznetsov, D. A.; Han, B.; Yu, Y.; Rao, R. R.; Hwang, J.; Roman-Leshkov, Y.; Shao-Horn, Y. Tuning Redox Transitions via Inductive Effect in Metal Oxides and Complexes, and Implications in Oxygen Electrocatalysis. *Joule* **2018**, *2*, 225−244.
(39) Walter, M. G.; Warren, E. L.; McKone, J. R.; Boettcher, S. W.; Mi, Q.; Santori, E. A.; Lewis, N. S. Solar Water Splitting Cells. *Chem. Rev.* **2010**, *110*, 6446−6473.
(40) Cherevko, S.; Geiger, S.; Kasian, O.; Kulyk, N.; Grote, J.-P.; Savan, A.; Shrestha, B. R.; Merzlikin, S.; Breitbach, B.; Ludwig, A.; Mayrhofer, K. J. J. Oxygen and Hydrogen Evolution Reactions on Ru, RuO2, Ir, and IrO2 Thin Film Electrodes in Acidic and Alkaline Electrolytes: A Comparative Study on Activity and Stability. *Catal. Today* **2016**, *262*, 170−180.
(41) Liu, X.; Chang, Z.; Luo, L.; Xu, T.; Lei, X.; Liu, J.; Sun, X. Hierarchical Zn x Co3−x O4 Nanoarrays with High Activity for Electrocatalytic Oxygen Evolution. *Chem. Mater.* **2014**, *26*, 1889−1895.

DOI: 10.1021/acsaem.9b00733
ACS Appl. Energy Mater. XXXX, XXX, XXX−XXX

(42) Zhou, T.; Cao, Z.; Zhang, P.; Ma, H.; Gao, Z.; Wang, H.; Lu, Y.; He, J.; Zhao, Y. Transition Metal Ions Regulated Oxygen Evolution Reaction Performance of Ni-Based Hydroxides Hierarchical Nanoarrays. *Sci. Rep.* **2017**, *7*, 46154−46162.
(43) Svane, A.; Gunnarsson, O. Transition-Metal Oxides in the Self-Interaction−Corrected Density-Functional Formalism. *Phys. Rev. Lett.* **1990**, *65*, 1148−1151.
(44) Alia, S. M.; Rasimick, B.; Ngo, C.; Neyerlin, K.; Kocha, S. S.; Pylypenko, S.; Xu, H.; Pivovar, B. S. Activity and Durability of Iridium Nanoparticles in the Oxygen Evolution Reaction. *J. Electrochem. Soc.* **2016**, *163*, F3105−F3112.
(45) Rong, F.; Zhao, J.; Su, P.; Yao, Y.; Li, M.; Yang, Q.; Li, C. Zinc−Cobalt Oxides as Efficient Water Oxidation Catalysts: the Promotion Effect of ZnO. *J. Mater. Chem. A* **2015**, *3*, 4010−4017.

DOI: 10.1021/acsaem.9b00733
ACS Appl. Energy Mater. XXXX, XXX, XXX−XXX